

# Concurrent Wireless Power Transfer and Motor Drive System with a Single Converter

Enes Ayaz, Oğün Altun, Hakan Polat, Furkan Karakaya, Ozan Keysan

**Abstract**—This paper presents a novel system to utilize conventional motor drives for wireless power transfer (WPT) to supply auxiliary systems such as IoT devices or sensors in rotating systems. The conventional method is to use a slip ring, which reduces reliability, or to use an extra high-frequency converter next to the motor drive, which increases the system cost. The development of wide-bandgap (WBG) devices such as GaN and SiC transistors has increased the switching frequencies of motor drives with lower switching losses. The voltage harmonics of these high switching frequencies can be utilized to excite a WPT system, while the low-frequency modulated current can still be used to drive the motor. In this paper, the relation between the motor drive and the WPT system is investigated under different operating conditions, and the proposed method is experimentally verified with a GaN-based full-bridge (FB) converter, a series-series (SS) WPT system at 50 W, and a DC motor at 500 W. Thereby, a cost-reduced contactless slip ring was obtained using the concurrent conventional motor drive and IPT systems.

**Index Terms**—Inductive Power Transfer(IPT), motor drivers, Wireless Power Transfer(WPT), slip rings, rotating systems

## I. INTRODUCTION

Power transfer to a rotating frame is required for many applications such as electrical excited synchronous machines [1], radar systems [2], internet of things (IoT) devices [3], sensors [4], etc. Slip rings, consisting of copper rings and carbon brushes in contact with these rings, can be used to excite these systems. However, they are unreliable and require periodic maintenance. Thanks to increased reliability, wireless power transfer (WPT) systems can be an alternative to slip rings [2], [5], [6]. The most common WPT type used for this kind of application is inductive power transfer (IPT) systems, which provide a flexible range of transfer distance with higher efficiencies.

In IPT systems, power is transferred by the magnetic coupling between the transmitter (Tx) and the receiver (Rx) coils, which are loosely coupled, resulting in inherently low power factors. Therefore, compensation circuits, such as two-element (series-series (SS), series-parallel (SP), parallel-parallel (PP), parallel-series (PS)) or hybrid compensation methods (LLC, LCC), are generally used [7]–[9]. Moreover, IPT systems require a high-frequency converter, such as half-bridge (HB) and full-bridge (FB) converters, to excite the Tx coils.

A conventional contactless slip ring using IPT systems is shown in Fig. 1.a. Such systems consist of two separate converters to drive the motor and excite the Tx coil. The

already existing motor drive in these systems generates high-frequency switching voltage harmonics, which are not desired, and attenuated in the motor phase currents due to high motor inductance. In the proposed system, the Tx coil utilizes these high-frequency voltage harmonics to transfer power to the Rx coil, while the low-frequency modulated current is still used to drive the motor. Thus, a separate IPT converter is no longer required, which reduces the complexity and cost of the overall system. The proposed system, shown in Fig. 1.b, can be used to excite auxiliary systems in the rotating frame for industrial applications such as IoT devices, surveillance cameras, robotic actuators, radars, sensors etc. Since the power ratings of these systems are lower than the power ratings of the main motor, it is possible to use existing conventional motor drive without any modifications.

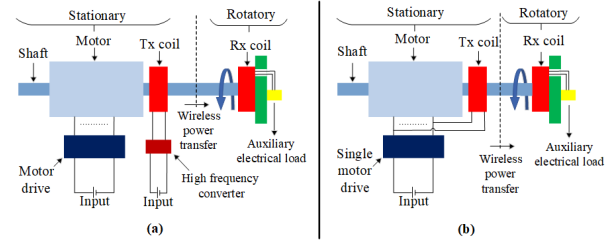


Fig. 1. IPT systems for rotating frames. a) A conventional IPT system. b) The proposed IPT system.

For conventional industrial motor drives, the switching frequency is usually below 20 kHz due to the switching losses of silicon (Si)-based transistors [10]. In this frequency range, IPT systems are not feasible since the Tx-Rx coils get bulkier as the frequency is reduced [11]. However, recent developments in semiconductor technology pave the way for higher switching frequencies (up to several hundred kHz), with Silicon Carbide (SiC) or Gallium Nitride (GaN) based motor drives [12], [13] while still achieving high efficiency [14]. Thus, it is now possible to utilize these high-frequency harmonics for IPT systems. The block diagram of the proposed system is presented in Fig. 2, and the advantages and disadvantages are discussed in Table I. The proposed system meets the requirements and solves the complexity and cost problem of the conventional systems that use two separate converters: one for the motor driver and one for IPT.

In this paper, a DC motor and an SS-IPT will be driven concurrently via a GaN-based FB converter as a proof of concept. The remaining parts of the paper are organized as follows. In section II, the theory of operation will be given for a DC motor and an IPT system. Section III will present

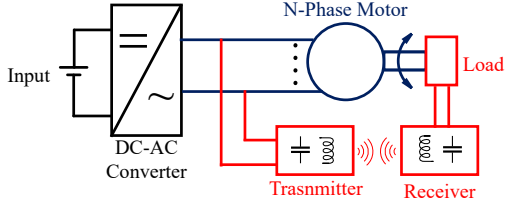


Fig. 2. The block diagram of the proposed IPT system utilizing existing motor drive.

TABLE I  
COMPARISON OF VARIOUS SYSTEMS TRANSFERRING POWER TO  
ROTATING SYSTEMS

	Mechanical Slip Rings	Conventional IPT Systems	The Proposed IPT System
Reliability	- [15]	+ [2]	+
Maintenance	- [16]	+	+
Simplicity	+	-	+
Cost Effective	+	-	+
Efficiency	+	+	+

the IPT system design steps and considerations. In section IV, the independent control method for the concurrent motor and the IPT systems are investigated. Section V will deliver the experimental results to validate analytical calculations. In Section VI, the system will be compared with existing studies in the literature. Section VII will discuss the soft-switching conditions and hardware-free implementation of the IPT system to conventional motor drives.

## II. THEORY OF OPERATION

In the proposed system, a separately excited DC motor and an IPT system are concurrently operated by a single FB converter, as shown in Fig. 3. The FB converter is driven by an asymmetrical bipolar PWM scheme, which generates DC output voltage with high-frequency switching harmonics. While the motor winding attenuates the high-frequency harmonics in motor current, the IPT systems amplify the switching frequency on the Tx coil. Besides, the DC voltage component that drives the motor is filtered out by IPT systems thanks to the series compensation capacitors. The switching function of the applied PWM is presented in (1), composing of switching frequency ( $f_s$ ), and duty cycle ( $D$ ). The harmonic

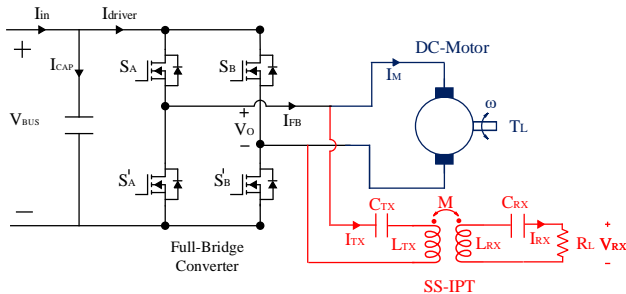


Fig. 3. Circuit diagram of the proposed concurrent motor drive and IPT systems with a single converter.

distribution of the converter output voltage for this PWM is given in Fig. 4.

$$S(t) = D + \sum_{k=1}^{\infty} \frac{2}{k\pi} \sin(k\pi D) \cos(2\pi k f_s t) \quad (1)$$

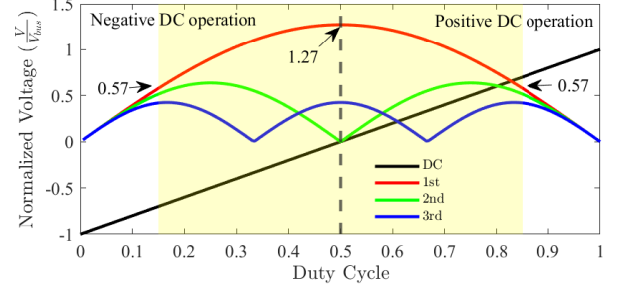


Fig. 4. The harmonic distribution of the converter's output voltage, which are obtained by analytically employing the switching function in the FB converter.

For duty cycle ( $D$ ) values less than 0.5, a negative DC output voltage is achieved. At  $D = 0.5$ , the DC output becomes zero, meaning that the power transferred to the motor is zero. For  $D > 0.5$ , a positive DC output voltage is obtained. Therefore, positive and negative DC output voltage levels can be obtained by varying the duty cycle and the motor speed and the rotation direction can be controlled.

The gate signals of top switches of each leg ( $S_A$  and  $S_B$ ), which are used to generate asymmetrical PWM, and converter voltage-current waveforms are represented in Fig. 5. The switching pattern generates a pulsating output voltage ( $V_o$ ), with a DC and switching components. The motor current ( $I_M$ ) is mainly DC with small current ripples. The Tx current ( $I_{TX}$ ) is sinusoidal by assuming that IPT has a high-quality factor. The FB converter current ( $I_{FB}$ ) is the sum of  $I_M$  and  $I_{TX}$ . However,  $I_{FB}$  is dominated by  $I_M$  since the IPT system is used for auxiliary systems, which have smaller power ratings than the motor.

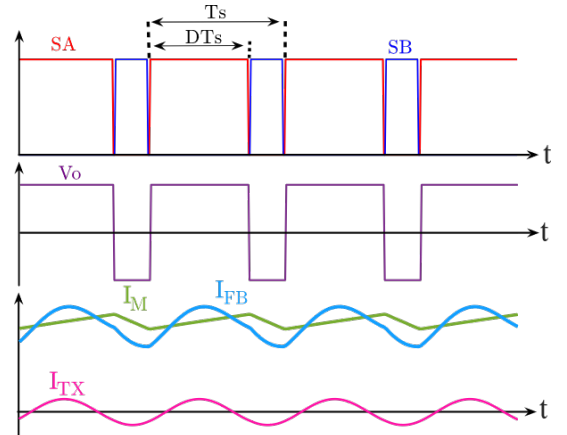


Fig. 5. Asymmetrical PWM signals and its corresponding voltage and current waveforms.

### III. SYSTEM DESIGN

The specifications of the system are given in Table II. The input voltage is selected as 100 V, and the motor rated power is 500 W while the rated power of the IPT system is 50 W with 20 V output voltage.

TABLE II

THE SYSTEM INPUT-OUTPUT SPECIFICATIONS AND THE PARAMETERS OF THE MOTOR AND THE DRIVER.

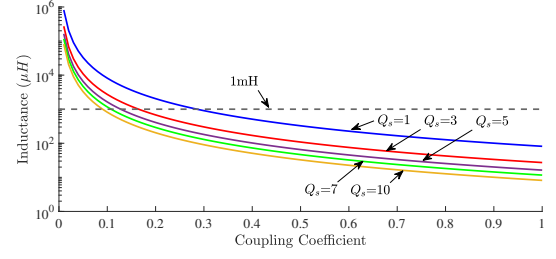
The Rated Voltages and Powers	
Input Voltage ( $V_{BUS}$ )	100 V <sub>DC</sub>
IPT Output Voltage ( $V_{RX}$ )	20 V <sub>RMS</sub>
Motor Output Power ( $P_M$ )	500 W
IPT Output Power ( $P_o$ )	50 W
The Motor Parameters	
Armature resistance ( $R_a$ )	2 $\Omega$
Armature inductance ( $L_a$ )	7 mH
Motor electrical time constant ( $T_s$ )	3.5 ms
The Driver Parameters	
Duty cycle ( $D$ )	0.15 – 0.85
Switching frequency ( $f_s$ )	< 100 kHz
Switching period ( $T_s$ )	> 10 $\mu$ s

#### A. Motor Drive

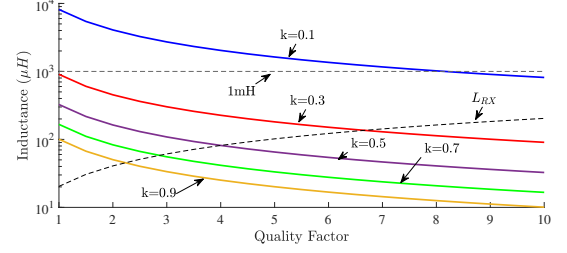
The motor drive system includes a separately excited DC machine and a GaN-based FB converter. The FB converter consists of two GaN-based half-bridge boards as details described in [17]. The motor and the drive parameters are given in Table II. Although the motor drive enables to use a switching frequency up to 100 kHz, there are some considerations to select the optimum switching frequency. On the one hand, increasing switching frequency increases the switching losses, which reduces the driver's lifetime. On the other hand, decreasing switching frequency increases the current and torque ripples. Moreover, increasing the switching frequency shrinks the passive components of the IPT system but increases the coil losses.

#### B. Inductive Power Transfer

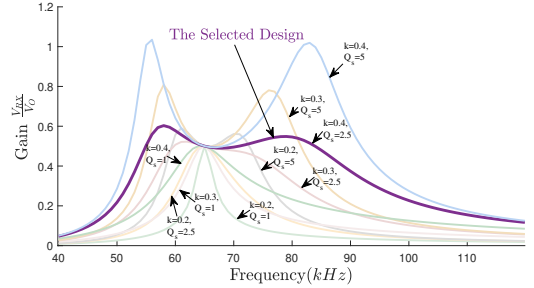
SS-IPT topology was preferred as the resonant frequency is independent of the load condition and mutual coupling. Since the IPT coils and the motor share the same converter in the proposed system, this independence gives control flexibility. The resonant frequency is selected as 65 kHz. Thus, the margin between 65 kHz and 100 kHz is used to control the output voltage by the frequency detuning method. As the motor driver is also used to excite the Tx coil, the input voltage of the IPT system (which is actually the first harmonic component for the output voltage of the FB converter) varies between 40 V<sub>RMS</sub> and 90 V<sub>RMS</sub> along with the duty cycle. For this reason, the design should be capable of delivering rated power over this wide range of the input voltage. A systematic design is accomplished for the minimum input voltage since the frequency detuning provides the ability to decrease power when the  $V_o$  is bigger than it [18]. Firstly, the Rx inductance can be calculated by using (2) where  $\omega_o$  is the resonant



(a) The inductance of the Tx coil as a function of  $k$ .



(b) The inductance of the Tx and Rx coils as a function of  $Q_{RX}$ .



(c) The gain-frequency characteristic of several  $k$  and  $Q_{RX}$ .

Fig. 6. Effect of the design parameters on Tx coil, Rx coil and gain of the IPT.

frequency in radian per second, and  $Q_{RX}$  is the quality factor,  $R_L$  is the load resistance.

$$L_{RX} = \frac{Q_{RX} R_L}{\omega_o} \quad (2)$$

$Q_{RX}$  should be between 2-10 as a rule of thumb [18], [19]. The higher  $Q_{RX}$  increases the size of the Rx coil but decreases the size of the Tx coil. Moreover, the mutual inductance can be calculated using (3) where  $V_{o,1st}$  is the first switching harmonic component for the output voltage of the FB converter.

$$M = \frac{V_{RX} V_{o,1st}}{P_o \omega_o} \quad (3)$$

The inductance of the Tx coil can be found using (4). The coupling coefficient ( $k$ ) varies between 0 and 1.

$$L_{TX} = \frac{V_{o,1st}^2}{k^2 \omega_o^2 Q_{RX}} \quad (4)$$

Finally, the capacitance values can be achieved using (5).

$$C_{TX,RX} = \frac{1}{L_{TX,RX} \omega_o^2} \quad (5)$$

IPT voltage gain characteristic depends on the selection of  $k$  and  $Q_{RX}$ . In regular IPT systems,  $k$  is limited to provide a bifurcation-free design, guaranteeing zero voltage

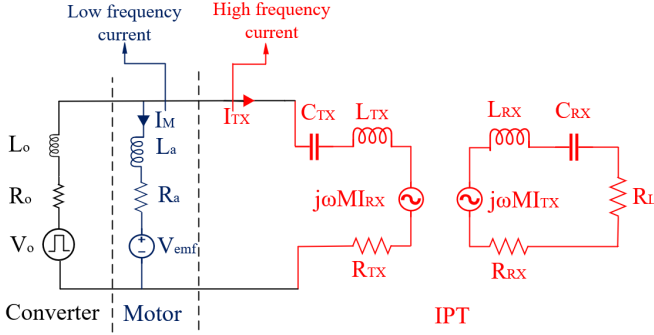


Fig. 7. Combined impedance model of the IPT system and the motor.

switching (ZVS) above the resonant frequency. However, ZVS may not be achieved in the proposed system due to the motor's current, which will be discussed later. Hence, bifurcation-free design is not aimed, and  $k$  should be selected considering the Tx coil inductance as shown in Fig. 6.a. Increasing  $k$  decreases the size of the Tx coil. Besides, the variations of Tx and Rx inductances as a function of  $Q_{RX}$  are shown in Fig. 6.b. Higher  $Q_{RX}$  increases the inductance of Rx coil, and decreases the inductance of Tx coil for a constant  $k$ . However,  $Q_{RX}$  and  $k$  also affect the gain-frequency characteristics, as shown in Fig. 6.c. Increasing both  $Q_{RX}$  and  $k$  leads the gain increase at two distinct resonants below and above the resonant frequency. The  $Q_{RX}$  and  $k$  are selected as 2.6 and 0.40 considering the size of Tx and Rx coils. The voltage gain at the resonant frequency is 0.5. In Table III, the finalized IPT system parameters are presented.

TABLE III  
PARAMETERS OF THE IPT SYSTEM AND THE RESONANCE ELEMENTS.

Receiver quality factor ( $Q_{RX}$ )	2.6
Resonant frequency ( $f_0$ )	65 kHz
Coupling factor ( $k$ )	0.40
Load resistance ( $R_L$ )	8 $\Omega$
Receiver coil inductance ( $L_{RX}$ )	51 $\mu$ H
Mutual inductance ( $M$ )	41 $\mu$ H
Transmitter coil inductance ( $L_{TX}$ )	205 $\mu$ H
Receiver resonant capacitance ( $C_{TX}$ )	115 nF
Transmitter resonant capacitance ( $C_{RX}$ )	29 nF
Airgap	10 mm
Coil diameter	110 mm

#### IV. IMPEDANCE MODELLING AND DECOUPLED CONTROL OF THE COMBINED MOTOR AND IPT SYSTEM

Fig. 7 shows the lumped circuit of the combined motor and the IPT system. The converter is modeled as a pulsating voltage source. Input impedances of the motor and the IPT are calculated as in (6) and (7), which are shown in Fig. 8.

$$Z_{in-M} = j\omega L_a + R_a \quad (6)$$

$$Z_{in-IPT} = j\omega L_{TX} + \frac{1}{j\omega C_{TX}} + R_{TX} + \frac{1}{\omega^2 M^2} \left( j\omega L_{RX} + \frac{1}{j\omega C_{RX}} + R_L + R_{RX} \right) \quad (7)$$

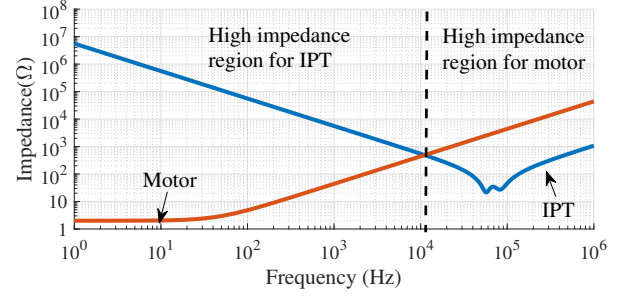
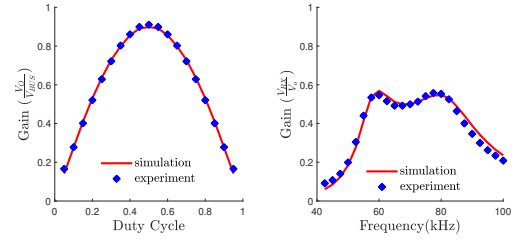
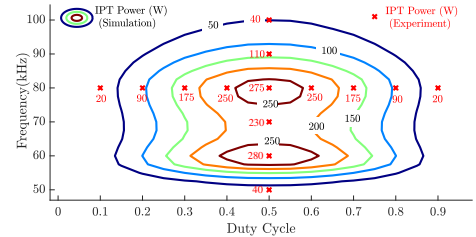


Fig. 8. Frequency response of the motor windings and the IPT coils.

$V_o$  consists of both DC and harmonics of the switching frequency. The switching frequency and IPT resonant frequency are selected compatible, so the IPT has low-impedance only at the switching frequency. Besides, the motor is like a low-pass filter, which leads the DC component to pass and the switching harmonics to attenuate. Thus, the operating frequencies of the motor and IPT system are far from each other. Furthermore, controls of the motor and the IPT system can be decoupled as they behave like high-impedance loads at each other's operating frequencies.



(a) Duty cycle-gain characteristic of IPT at 80 kHz. (b) Frequency-gain characteristic of IPT ( $D = 0.5$ ).



(c) The iso-power lines of IPT through duty cycle and frequency.

Fig. 9. Simulation and experimental results of IPT voltage gain and power as a function of duty cycle and frequency.

The motor current is controlled by varying the duty cycle, and it is independent of the switching frequency, whereas the gain of SS-IPT is changed by both the duty cycle and the frequency. The variation of the output voltage of SS-IPT (at  $f_{sw}=80$  kHz) along with the duty cycle is shown in Fig. 9.a, and the variation of the output voltage with the switching frequency (with  $D=0.5$ ) is shown in Fig. 9.b. On account of this, the power of IPT is plotted for different duty cycles and frequencies in Fig. 9.c, and it is observed that IPT power is kept constant by appropriate choice of the duty cycle and the switching frequency.



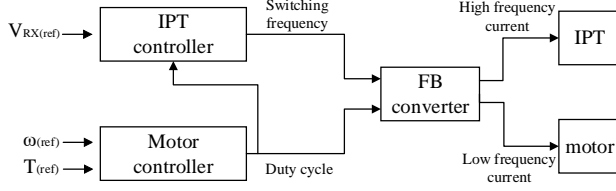


Fig. 11. The block diagram of the control method of the combined motor and IPT system.

Consequently, the overall control method for the proposed system is given in Fig. 11. The motor controller decides on the duty cycle, considering the speed and torque. Then, the IPT controller adjusts the switching frequency to obtain desired output voltage of the IPT system for the changing duty cycle.

## V. EXPERIMENTAL RESULTS

The experimental results are obtained using the setup, consisting of a DC motor with a GaN-based motor drive where the parameters are given in Table II, a generator, an IPT system where the parameters are given in Table III, a DC supply, and an oscilloscope. The setup is shown in Fig. 12.

### A. IPT Tests

IPT coils are wound, and the inductances are achieved as shown in Table IV. Firstly, the gain of  $V_{o,1st}$  over the DC link voltage is obtained at  $f_{sw} = 80 kHz$ . Then, the gain of the IPT system is attained at  $D = 0.5$ . The simulation results are compared with the experimental results, shown in Fig. 9. The experimental results have an agreement with simulation results as expected.

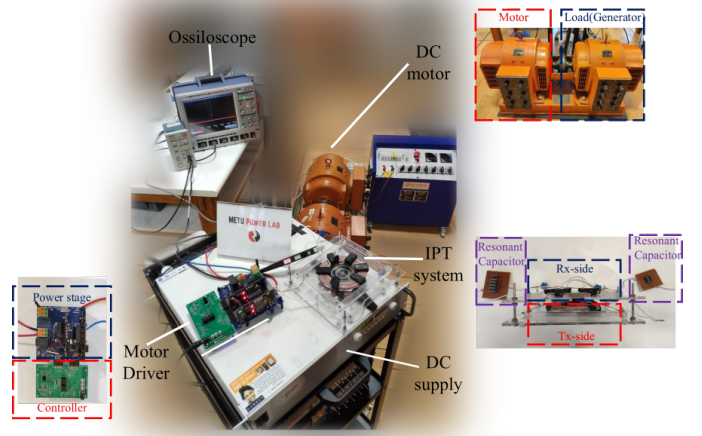


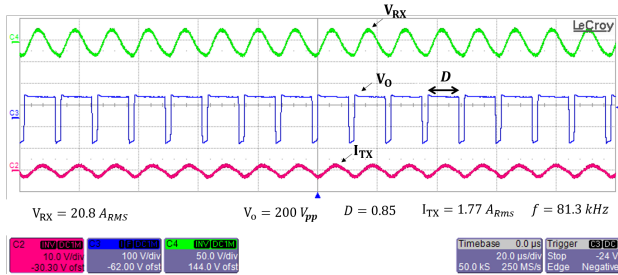
Fig. 12. The illustration of experimental setup.

TABLE IV  
SYSTEM PARAMETERS OF THE SS-IPT

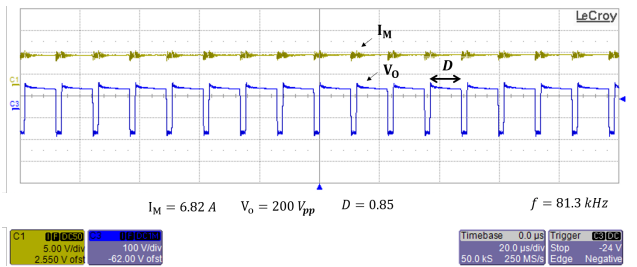
Transmitter inductance	205 $\mu H$
Receiver inductance	51 $\mu H$
Mutual inductance	40 $\mu H$

### B. Concurrent operation of the IPT and the motor

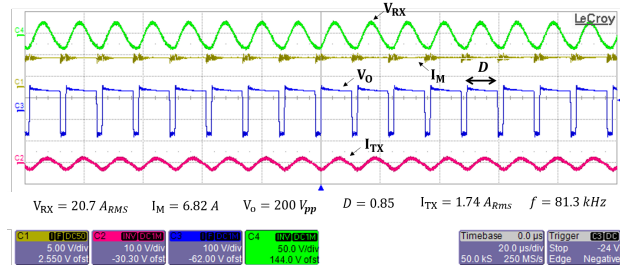
In order to test the relation between the motor and IPT system, firstly, only the IPT system is connected to the FB converter, and the system operates at  $f_{sw} = 81.3 kHz$  with  $D=0.85$ . Fig. 10.a shows the output voltage of IPT ( $V_{RX}$ ), the output voltage of FB converter ( $V_o$ ) and the transmitter coil current ( $I_{TX}$ ). IPT system transfers 54 W power at 20.8  $V_{RMS}$



(a)  $I_{TX}$ ,  $V_{RX}$  and  $V_o$  for single IPT operation.



(b)  $I_M$  and  $V_o$  for single motor operation.



(c)  $I_{TX}$ ,  $I_M$ ,  $V_{RX}$  and  $V_o$  for simultaneous the IPT and the motor operations.

Fig. 10. Experimental results of the concurrent operation of the proposed system with 100 V DC-link.

at this operation point. Secondly, only the motor is connected to the FB converter with the same duty cycle and switching frequency. Fig. 10.b shows the  $V_o$  and motor current ( $I_M$ ). For this operation point, 480 W is delivered to the motor. Finally, the motor and IPT system are connected concurrently to the FB converter, and it operates at the same conditions. In Fig. 10.c,  $V_{RX}$ ,  $I_M$ ,  $V_o$ , and  $I_{TX}$  are shown. It is observed that the motor current and the power delivered to the motor are not affected from the IPT system. In addition, the output voltage of the IPT stays constant with or without the motor. Although these initial results imply that the IPT system and the motor operations do not affect each other, the proposed system should be verified at different operating conditions.

### C. Loss and Efficiency Measurements

One challenge of the proposed method is the additional high-frequency current components that need to be carried by the converter, which may create extra thermal stress. Thus, the effect of the proposed system on drive losses needs to be examined. As these loss components are small and it is difficult to measure using electrical measurements, a calorimeter, which is regarded as more accurate than electrical loss calculations [20], is utilized. The total power loss in the drive for three conditions given in the previous subsection are measured, and they are presented in Table V.

TABLE V  
EXPERIMENTAL RESULTS OF THE CONVERTER'S LOSS AND EFFICIENCY ANALYSIS WITH A CALORIMETER

Operation	Input Power (W)	Driver Losses (W)	Converter Output Power (W)	Efficiency (%)
Only IPT	67.6	7.3	60.3	89.2
Only Motor	457.1	12.8	444.3	97.2
IPT and Motor	522.2	14.1	508.1	97.3

The drive loss of simultaneous operation increases only 10% compared to the only motor operation, and so the system is feasible concerning thermal management.

### D. The effect of transient load variations

In order to observe the transient response of the motor and IPT system, loads of each system is suddenly increased and decreased while keeping the other parameters constant. The motor and Rx currents are shown in Fig.13, and responses will be explained for each time interval as follows:

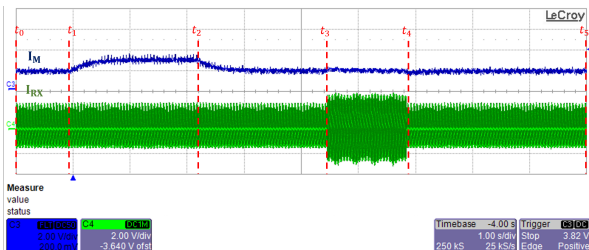


Fig. 13. Experiment results for transient load variations of motor and IPT system.

- $t_0 - t_1$ : The motor is loaded with 105 W ( $I_m = 1.9$  A), and the IPT system transmits 35 W ( $I_{RX} = 1.7$  A<sub>RMS</sub>).
- $t_1$ : The power of the motor raises to 171 W.
- $t_1 - t_2$ :  $I_m$  reaches to 2.9 A while  $I_{RX}$  is constant at 1.7 A<sub>RMS</sub>.
- $t_2$ : The power of the motor reduces to 105 W.
- $t_2 - t_3$ :  $I_m$  reduces to 1.9 A while  $I_{RX}$  is constant at 1.7 A<sub>RMS</sub>.
- $t_3$ : The IPT system power increases to 63 W.
- $t_3 - t_4$ : While  $I_m$  is kept constant at 1.9 A,  $I_{RX}$  increases to 2.4 A<sub>RMS</sub>.
- $t_4$ : The IPT power decreases to 35 W.
- $t_4 - t_5$ : While  $I_m$  is constant at 1.9 A,  $I_{RX}$  reduces to 1.7 A<sub>RMS</sub>.

These tests prove the independent operation of IPT and motor. The operation of the IPT system is not disturbed by the motor load variations. The motor current is slightly affected ( by a 5% overshoot or undershoot ) at transients of the IPT system, but it quickly reaches the steady-state value as expected.

### E. Tests under different operating conditions

In order to further investigate the operation range of the proposed system, seven different operating points are selected. The duty cycles and switching frequency are adjusted to provide the desired power of the motor and IPT system as shown in Fig. 11. Table VI presents the test parameters for each case.

TABLE VI  
CONCURRENT OPERATION OF THE IPT AND THE MOTOR UNDER DIFFERENT OPERATING CONDITIONS.

	Cases						
	A	B	C	D	E	F	G
Frequency (kHz)	95	90	90	95	90	90	97.5
Duty Cycle	0.6	0.75	0.75	0.6	0.6	0.6	0.5
Load Torque (N.m)	0.24	0.27	0.37	0.21	0.21	0.17	-
Motor Power (W)	125	179	244	109	110	89	-
IPT Power (W)	50	51	51	50	90	90	52.7

- : The load torque and motor power do not exist due to the motor speed being zero at  $D = 0.5$ .

The power of the motor and IPT systems are shown in Fig 14. It is shown that the IPT power can be kept constant by frequency detuning for two different duty cycles as in the transition from A to B. In addition, the transitions from B to C and from E to F show that the IPT powers stay constant for two different motor loadings with the same duty cycle and switching frequency. Moreover, the motor power is not affected by the switching frequency variations, which is shown in the transition from D to E. Finally, duty cycle is brought to 0.5 in operating condition G, where the converter stops the motor. At this operating condition, it is observed that the IPT system still transfers the required minimum power. It is concluded that the IPT system and motor can operate for

[illegible]

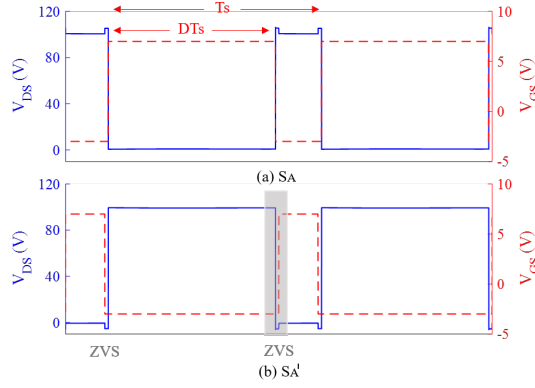


Fig. 16. Drain-source and gate-source voltage waveforms at  $D = 0.8$  and  $f = 80\text{kHz}$  for dominant motor current conditions.

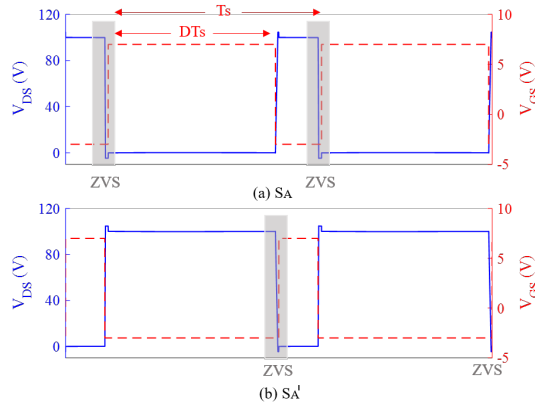


Fig. 17. Drain-source and gate-source voltage waveforms at  $D = 0.8$  and  $f = 80\text{kHz}$  for dominant IPT current conditions.

2)  $I_M < \hat{I}_{TX}$ : While the motor current is less than the peak of the IPT current, the converter current changes the sign in a switching period. Thus, both switches of each leg can sustain ZVS depending on the magnitude of currents and the phase of IPT currents. An example of ZVS is presented in Fig. 17 for  $S_A$  and  $S_{A'}$  switches. To conclude, when the motor current is dominant, the soft-switching conditions do not change due to the addition of the IPT current. However, for light motor loads, ZVS condition at one switch of each leg may be missing, but it is not expected to cause thermal or efficiency issues for these conditions. Moreover, the system can still sustain a ZVS on both legs when the peak of the IPT current is greater than the motor current.

### B. The stress on the DC-link Capacitor

Unlike a conventional motor drive, the addition of the high-frequency IPT current on the motor driver also increases the stress on the DC-link capacitor. Hence, adding the IPT system to a conventional motor drive may require minor modifications to the DC-link capacitance or to the type of capacitors. The current, supplied by the DC-link capacitors ( $I_{CAP}$ ), is expressed as in (9) using switching functions ( $S_A$  and  $S_B$ ) for the converter legs.

$$I_{CAP} = S_A(I_M + I_{TX}) - S_B(I_M + I_{TX}) - I_{in} \quad (9)$$

The motor and IPT currents ( $I_M$  and  $I_{TX}$ ) are shown in (10). The switching harmonics of the motor current can be ignored ( $I_{Mdc}$ ), and the first harmonic approximation (FHA) can be applied to the IPT current ( $I_{TXf}$ ).

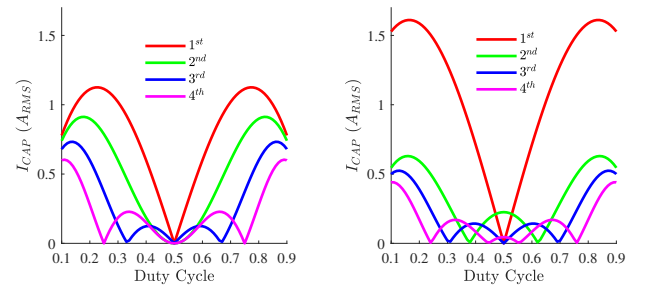
$$\begin{aligned} I_M &= I_{Mdc} \\ I_{TX} &= I_{TXf} \cos(2\pi f_s t - \Phi) \end{aligned} \quad (10)$$

The DC-link current harmonic components of the motor and IPT system can be obtained as in (11) and (12). Therefore, the DC-link current depends on the motor current, duty cycle, and Tx current.

$$I_{capM} = \sum_{k=1}^{\infty} \frac{4I_{Mdc}}{k\pi} \sin(k\pi D) \cos(2\pi k f_s t) \quad (11)$$

$$\begin{aligned} I_{capTX} &= -I_{TX} \cos(2\pi f_s t - \Phi) \\ &+ \sum_{k=1}^{\infty} \frac{2I_{TX}}{k\pi} \sin(k\pi D) \cos(2\pi(k+1)f_s t - \Phi) \\ &+ \sum_{k=2}^{\infty} \frac{2I_{TX}}{k\pi} \sin(k\pi D) \cos(2\pi(k-1)f_s t + \Phi) \end{aligned} \quad (12)$$

Since the capacitor current is affected by the motor current and duty cycle, a worst-case scenario is analyzed for simplicity. In this scenario, the motor current is initially zero at  $D = 0.5$ , and the motor power is linearly increased up to 500 W at  $D = 0.85$ . The DC-link current can be calculated as in (11) when just the motor is connected. Then, the IPT system is connected parallel to the motor. The IPT system supplies 50W power while the duty cycle is varied from 0.15 to 0.85. The capacitor current, which stems from the IPT system, is calculated using (12). The capacitor currents for single and combined operation mode are shown in Fig. 18. The capacitor current changes with the duty cycles. Whereas the first switching harmonics are increased after the connection of the IPT system, it is observed that the higher harmonics are decreased.



(a) DC-link current under single motor operation. (b) DC-link current under combined motor and IPT operation.

Fig. 18. First, second, third and fourth harmonics of the DC link currents as a function of duty cycle.

After connecting the IPT system, the capacitor current increases from  $1.45 \text{ A}_{RMS}$  to  $1.8 \text{ A}_{RMS}$ , resulting in a 24% rise. Therefore, this may require minor modifications in capacitance if the IPT system is implemented to a conventional motor driver.



## VIII. CONCLUSION

In this article, a novel IPT system to transfer power to rotating frames has been proposed. Unlike conventional systems, the proposed method does not require an extra converter, and the already existing motor driver is utilized to concurrently run the motor and transfer power wirelessly. Hence, the complexity and cost are decreased. However, choosing a proper switching frequency is challenging since a high switching frequency increases the converter losses, and a low switching frequency increases the IPT coil size and cost. With the development of wide band-gap devices such as GaN and SiC, a sweet spot could be found, satisfying both requirements. Thus, the wide band-gap drives can be used as a single converter for concurrent operations of motor and IPT systems. DC-link capacitor stress due to the extra IPT system has been investigated in this study, and it was concluded that the IPT system could be implemented to any conventional motor drive with maybe a slight modification to the DC-link capacitors. Although the proposed system is tested on a conventional DC motor, the same method can be extended for several industrial applications such as field-excitation of multi-phase synchronous AC machines, BLDC motors, etc.

## REFERENCES

- [1] M. Maier and N. Parspour, "Operation of an electrical excited synchronous machine by contactless energy transfer to the rotor," *IEEE Transactions on Industry Applications*, vol. 54, no. 4, pp. 3217–3225, 2018.
- [2] G. He, Q. Chen, X. Ren, S. Wong, and Z. Zhang, "Modeling and design of contactless slippings for rotary applications," *IEEE Transactions on Industrial Electronics*, vol. 66, no. 5, pp. 4130–4140, 2019.
- [3] M. Markiewicz, M. Wielgosz, M. Bocheński, W. Tabaczyński, T. Konieczny, and L. Kowalczyk, "Predictive maintenance of induction motors using ultra-low power wireless sensors and compressed recurrent neural networks," *IEEE Access*, vol. 7, pp. 178 891–178 902, 2019.
- [4] G. Lee, H. Gwak, Y.-S. Kim, and W.-S. Park, "Wireless power transfer system for diagnostic sensor on rotating spindle," in *2013 IEEE Wireless Power Transfer (WPT)*, 2013, pp. 100–102.
- [5] M. R. Barzegaran, H. Zargarzadeh, and O. A. Mohammed, "Wireless power transfer for electric vehicle using an adaptive robot," *IEEE Transactions on Magnetics*, vol. 53, no. 6, pp. 1–4, 2017.
- [6] H. Polat, "Fault tolerant modular inductive power transfer system design using resonator coil," Apr 2021. [Online]. Available: [https://www.techrxiv.org/articles/preprint/Fault\\_Tolerant\\_Modular\\_Inductive\\_Power\\_Transfer\\_System\\_Design\\_Using\\_Resonator\\_Coil/14370617/1](https://www.techrxiv.org/articles/preprint/Fault_Tolerant_Modular_Inductive_Power_Transfer_System_Design_Using_Resonator_Coil/14370617/1)
- [7] Y. H. Sohn, B. H. Choi, E. S. Lee, G. C. Lim, G. Cho, and C. T. Rim, "General unified analyses of two-capacitor inductive power transfer systems: Equivalence of current-source ss and sp compensations," *IEEE Transactions on Power Electronics*, vol. 30, no. 11, pp. 6030–6045, 2015.
- [8] J. Zeng, G. Zhang, S. S. Yu, B. Zhang, and Y. Zhang, "Llc resonant converter topologies and industrial applications — a review," *Chinese Journal of Electrical Engineering*, vol. 6, no. 3, pp. 73–84, 2020.
- [9] X. Qu, H. Chu, S. Wong, and C. K. Tse, "An ipt battery charger with near unity power factor and load-independent constant output combating design constraints of input voltage and transformer parameters," *IEEE Transactions on Power Electronics*, vol. 34, no. 8, pp. 7719–7727, 2019.
- [10] S. Tiwari, O. . Midtgård, and T. M. Undeland, "Sic mosfets for future motor drive applications," in *2016 18th European Conference on Power Electronics and Applications (EPE'16 ECCE Europe)*, 2016, pp. 1–10.
- [11] V. Shevchenko, O. Husev, R. Strzelecki, B. Pakhaliuk, N. Poliakov, and N. Strzelecka, "Compensation topologies in ipt systems: Standards, requirements, classification, analysis, comparison and application," *IEEE Access*, vol. 7, pp. 120 559–120 580, 2019.
- [12] A. K. Morya, M. C. Gardner, B. Anvari, L. Liu, A. G. Yepes, J. Doval-Gandoy, and H. A. Toliyat, "Wide bandgap devices in ac electric drives: Opportunities and challenges," *IEEE Transactions on Transportation Electrification*, vol. 5, no. 1, pp. 3–20, 2019.
- [13] W. Lee, S. Li, D. Han, B. Sarlioglu, T. A. Minav, and M. Pietola, "A review of integrated motor drive and wide-bandgap power electronics for high-performance electro-hydrostatic actuators," *IEEE Transactions on Transportation Electrification*, vol. 4, no. 3, pp. 684–693, 2018.
- [14] E. A. Jones, F. F. Wang, and D. Costinett, "Review of commercial gan power devices and gan-based converter design challenges," *IEEE Journal of Emerging and Selected Topics in Power Electronics*, vol. 4, no. 3, pp. 707–719, 2016.
- [15] D. C. Ludois, J. K. Reed, and K. Hanson, "Capacitive power transfer for rotor field current in synchronous machines," *IEEE Transactions on Power Electronics*, vol. 27, no. 11, pp. 4638–4645, 2012.
- [16] J. Dai, S. Hagen, D. C. Ludois, and I. P. Brown, "Synchronous generator brushless field excitation and voltage regulation via capacitive coupling through journal bearings," *IEEE Transactions on Industry Applications*, vol. 53, no. 4, pp. 3317–3326, 2017.
- [17] F. Karakaya, O. S. Alemdar, and O. Keysan, "Layout Based Ultra-Fast Short-Circuit Protection Technique for Parallel Connected GaN HEMTs," *IEEE Journal of Emerging and Selected Topics in Power Electronics*, pp. 1–1, 2021.
- [18] K. Aditya and S. S. Williamson, "Design guidelines to avoid bifurcation in a series-series compensated inductive power transfer system," *IEEE Transactions on Industrial Electronics*, vol. 66, no. 5, pp. 3973–3982, 2019.
- [19] G. A. Covic and J. T. Boys, "Modern trends in inductive power transfer for transportation applications," *IEEE Journal of Emerging and Selected Topics in Power Electronics*, vol. 1, no. 1, pp. 28–41, 2013.
- [20] D. Christen, U. Badstuebner, J. Biela, and J. W. Kolar, "Calorimetric power loss measurement for highly efficient converters," in *The 2010 International Power Electronics Conference - ECCE ASIA -*, 2010, pp. 1438–1445.
- [21] J.-N. Weber, A. Rehfeldt, S.-A. Vip, and B. Ponick, "Rotary transformer with electrical steel core for brushless excitation of synchronous machines," in *2016 XXII International Conference on Electrical Machines (ICEM)*, 2016, pp. 884–889.
- [22] J. Dai, S. Hagen, D. C. Ludois, and I. P. Brown, "Synchronous generator brushless field excitation and voltage regulation via capacitive coupling through journal bearings," *IEEE Transactions on Industry Applications*, vol. 53, no. 4, pp. 3317–3326, 2017.
- [23] D. Maier, J. Kurz, and N. Parspour, "Contactless energy transfer for inductive electrically excited synchronous machines," in *2019 IEEE PELS Workshop on Emerging Technologies: Wireless Power Transfer (WoW)*, 2019, pp. 191–195.
- [24] K. D. Papastergiou and D. E. Macpherson, "An airborne radar power supply with contactless transfer of energy—part i: Rotating transformer," *IEEE Transactions on Industrial Electronics*, vol. 54, no. 5, pp. 2874–2884, 2007.
- [25] D. C. Ludois, M. J. Erickson, and J. K. Reed, "Aerodynamic fluid bearings for translational and rotating capacitors in noncontact capacitive power transfer systems," *IEEE Transactions on Industry Applications*, vol. 50, no. 2, pp. 1025–1033, 2014.
- [26] W. Zhou, "Design and analysis of decoupled tetra-polar ring-coils for wireless power transfer in rotary mechanism applications," *IET Electric Power Applications*, vol. 14, pp. 1766–1773(7), October 2020. [Online]. Available: <https://digital-library.theiet.org/content/journals/10.1049/iet-epa.2019.1000>
- [27] L. Sun, J. Kang, Y. Liu, Z. Mao, and Z. Zhong, "Wireless power transfer based contactless excitation of electrically excited synchronous motor," in *2020 IEEE 9th International Power Electronics and Motion Control Conference (IPEMC2020-ECCE Asia)*, 2020, pp. 1091–1097.
- [28] X. Feng, Z. Fu, G. Hao, K. Wang, and Y. Weng, "Modeling and implementation of a new non-contact slip ring for wireless power transfer," in *2020 IEEE 9th International Power Electronics and Motion Control Conference (IPEMC2020-ECCE Asia)*, 2020, pp. 106–111.
- [29] K. Song, B. Ma, G. Yang, J. Jiang, R. Wei, H. Zhang, and C. Zhu, "A rotation-lightweight wireless power transfer system for solar wing driving," *IEEE Transactions on Power Electronics*, vol. 34, no. 9, pp. 8816–8830, 2019.
- [30] R. Trevisan and A. Costanzo, "A 1-kw contactless energy transfer system based on a rotary transformer for sealing rollers," *IEEE Transactions on Industrial Electronics*, vol. 61, no. 11, pp. 6337–6345, 2014.
- [31] C. Zhang, D. Lin, and S. Y. R. Hui, "Ball-joint wireless power transfer systems," *IEEE Transactions on Power Electronics*, vol. 33, no. 1, pp. 65–72, 2018.